

Article

Intercalated PtCo Electrocatalyst of Vanadium Metal Oxide Increases Charge Density to Facilitate Hydrogen Evolution

Jingjing Zhang ¹, Wei Deng ^{1,*}, Yun Weng ², Jingxian Jiang ¹, Haifang Mao ¹, Wenqian Zhang ¹, Tiandong Lu ¹, Dewu Long ³ and Fei Jiang ^{1,*} 

¹ School of Chemical and Environmental Engineering, Shanghai Institute of Technology, Shanghai 201418, China; zhangjingjingsit@126.com (J.Z.); jjx@sit.edu.cn (J.J.); maohaifang2000@126.com (H.M.); zhangwq2004@163.com (W.Z.); lutandong2003@163.com (T.L.)

² State Key Laboratory for Modification of Chemical Fibers and Polymer Materials, College of Textile, Donghua University, Shanghai 201620, China; wendy_weng@163.com

³ Key Laboratory in Interfacial Physics and Technology, Shanghai Institute of Applied Physics, Chinese Academy of Sciences, Shanghai 201800, China; longdewu2010@126.com

* Correspondence: wdeng@sit.edu.cn (W.D.); jiangfei@sit.edu.cn (F.J.)

Abstract: Efforts to develop high-performance electrocatalysts for the hydrogen evolution reaction (HER) are of utmost importance in ensuring sustainable hydrogen production. The controllable fabrication of inexpensive, durable, and high-efficient HER catalysts still remains a great challenge. Herein, we introduce a universal strategy aiming to achieve rapid synthesis of highly active hydrogen evolution catalysts using a controllable hydrogen insertion method and solvothermal process. Hydrogen vanadium bronze $H_xV_2O_5$ was obtained through controlling the ethanol reaction rate in the oxidization process of hydrogen peroxide. Subsequently, the intermetallic PtCoVO supported on two-dimensional graphitic carbon nitride ($g-C_3N_4$) nanosheets was prepared by a solvothermal method at the oil/water interface. In terms of HER performance, PtCoVO/ $g-C_3N_4$ demonstrates superior characteristics compared to PtCo/ $g-C_3N_4$ and PtCoV/ $g-C_3N_4$. This superiority can be attributed to the notable influence of oxygen vacancies in $H_xV_2O_5$ on the electrical properties of the catalyst. By adjusting the relative proportions of metal atoms in the PtCoVO/ $g-C_3N_4$ nanomaterials, the PtCoVO/ $g-C_3N_4$ nanocomposites show significant HER overpotential of $\eta_{10} = 92$ mV, a Tafel slope of 65.21 mV dec^{-1} , and outstanding stability (a continuous test lasting 48 h). The nanoarchitecture of a $g-C_3N_4$ -supported PtCoVO nanoalloy catalyst exhibits exceptional resistance to nanoparticle migration and corrosion, owing to the strong interaction between the metal nanoparticles and the $g-C_3N_4$ support. Pt, Co, and V simultaneous doping has been shown by Density Functional Theory (DFT) calculations to enhance the density of states (DOS) at the Fermi level. This augmentation leads to a higher charge density and a reduction in the adsorption energy of intermediates.

Keywords: hydrogen evolution reaction; electrocatalysts; polymetallic compounds; hydrogen metal oxide bronzes



Citation: Zhang, J.; Deng, W.; Weng, Y.; Jiang, J.; Mao, H.; Zhang, W.; Lu, T.; Long, D.; Jiang, F. Intercalated PtCo Electrocatalyst of Vanadium Metal Oxide Increases Charge Density to Facilitate Hydrogen Evolution.

Molecules **2024**, *29*, 1518. <https://doi.org/10.3390/molecules29071518>

Academic Editor: Xiaomin Xu

Received: 27 January 2024

Revised: 16 March 2024

Accepted: 18 March 2024

Published: 28 March 2024



Copyright: © 2024 by the authors. Licensee MDPI, Basel, Switzerland. This article is an open access article distributed under the terms and conditions of the Creative Commons Attribution (CC BY) license (<https://creativecommons.org/licenses/by/4.0/>).

1. Introduction

To resolve the global energy crisis, the desirable search for renewable energy sources to substitute traditional fossil energy has attracted wide attention all over the world, including metal–air batteries, fuel cells, and electrochemical water decomposition [1,2]. The clean, renewable, and abundant nature of hydrogen energy positions it as one of the most promising energy carriers [3,4]. Over the past dozen years, electrocatalysts including oxides and alloys [5,6], phosphide [7,8], nitrides [9,10], selenides [11], and carbides [12,13] have shown remarkable HER activity. However, high-efficient, low-cost electrochemical water splitting development still faces great challenges.

Traditional hydrogen production strategies cannot avoid the emission of carbon dioxide, while electrically driven water splitting technology is a promising technology for

hydrogen production [14–16]. In the process of water electrolysis, concerning how to obtain high-energy density and pure hydrogen effectively and reduce the overpotential, electrocatalysts play a crucial role. Over the past few decades, platinum (Pt)-based noble metals have been considered benchmark HER electrocatalysts which exhibit extremely low overpotential [17]. In spite of the positive features of Pt-based electrocatalysts, the great number of inconveniences (hard to synthesize) and shortcomings (low abundance and high price) still impede their practical applications [18]. Consequently, it is particularly desirable to seek high-efficient and durable catalysts for water electrolysis to reduce noble Pt content and overpotential, thus improving the energy conversion efficiency [19].

In this study, we present a novel method utilizing hydrogen insertion vanadium powder (V) to manipulate the reaction rate of hydrogen peroxide (H_2O_2) in the presence of ethanol. By controlling the reaction rate through the presence of ethanol, we can successfully obtain hydrogen metal oxide bronzes (HVOs), such as hydrogen vanadium bronze. Moreover, the HVOs exhibit excellent dispersion and stability in solvents devoid of water, specifically alcoholic-based solvents. This characteristic is highly advantageous for enhancing device stability and facilitating processing. Previous reports have shown that coupling metal nanoparticles with carbon substrates can effectively improve electrocatalytic performance and enhance stability due to the effective surface corrosion inhibition and excellent electron transport properties of carbon materials [20]. Therefore, $\text{g-C}_3\text{N}_4$ is chosen as the substrate in this study. Subsequently, the intermetallic PtCoVO anchored on two-dimensional $\text{g-C}_3\text{N}_4$ nanosheets is prepared by a one-pot solvothermal process at the oil/water interface. The PtCoVO/ $\text{g-C}_3\text{N}_4$ catalyst, prepared in the aforementioned manner, demonstrates exceptional performance in the HER, which can be attributed to the substantial impact of oxygen vacancies present in HVOs on the electrical properties of the catalyst, resulting in enhanced HER performance [21]. As anticipated, the PtCoVO/ $\text{g-C}_3\text{N}_4$ catalyst demonstrates excellent performance in an alkaline HER, showcasing a low overpotential of $\eta_{10} = 92$ mV and a small Tafel slope of 65.21 mV dec^{-1} . Additionally, the catalyst exhibits remarkable stability, comparable to the near state-of-the-art Pt/C 20% catalyst (90.6 mV, 10 mA cm^{-2}). Detailed structural investigations reveal that the hydrogen insertion strategy modulates the effect of oxygen content in HVOs on electrical properties, which might result in a special V active center that enhances HER activity.

2. Results and Discussion

2.1. Morphologies and Structures

The tunable polymetallic nanocomposites PtCoVO/ $\text{g-C}_3\text{N}_4$ were successfully synthesized through a solvothermal method, as illustrated in Figure 1, which utilized three kinds of metal precursors, cobalt acetylacetonate ($\text{Co}(\text{acac})_3$), $\text{H}_2\text{PtCl}_6 \cdot 6\text{H}_2\text{O}$, and vanadium bronze (here, we use $\text{H}_x\text{V}_2\text{O}_5$ to represent HVOs), grown on two-dimensional $\text{g-C}_3\text{N}_4$ nanosheets. In particular, the unique low-temperature solution-processed hydrogen vanadium bronze $\text{H}_x\text{V}_2\text{O}_5$ was synthesized through a regulable hydrogen insertion method. Under ambient temperature conditions, vanadium powder was gradually oxidized by H_2O_2 in the existence of ethanol. Through the carefully controlled, sluggish reaction rate facilitated by ethanol, the solution-processed hydrogen metal oxide bronze $\text{H}_x\text{V}_2\text{O}_5$ was successfully obtained [22]. The $\text{H}_x\text{V}_2\text{O}_5$ color changed from yellow to brown during the preparation process, as can be seen in Figure S1. Subsequently, the polymetallic PtCoVO supported on two-dimensional $\text{g-C}_3\text{N}_4$ nanosheets was synthesized by using a one-pot solvothermal method at the oil/water interface. The enlarged PtCoVO surface structure was selected as the computational model for the illustration of as-prepared PtCoVO/ $\text{g-C}_3\text{N}_4$ electrocatalysts. For the purpose of comparison, our focus was directed toward three distinct materials with varying chemical compositions that were prepared in advance: PtCo/ $\text{g-C}_3\text{N}_4$, PtCoV/ $\text{g-C}_3\text{N}_4$, and PtCoVO/ $\text{g-C}_3\text{N}_4$, respectively. We utilized V powder to directly prepare PtCoV/ $\text{g-C}_3\text{N}_4$ to compare the different influences between V powder and $\text{H}_x\text{V}_2\text{O}_5$ bronzes. (Here, we denote PtCo/ $\text{g-C}_3\text{N}_4$ as prepared by adding no vanadium, PtCoV/ $\text{g-C}_3\text{N}_4$ as prepared by adding V powder, and PtCoVO/ $\text{g-C}_3\text{N}_4$ as prepared by

$H_xV_2O_5$) By adjusting the metal atoms, Pt, Co, and V, to appropriate molar ratio, the composite materials were meticulously optimized to achieve desired tunability in the elemental components. A detailed description of the synthesis process for composites with varying proportions is provided in the experimental section.

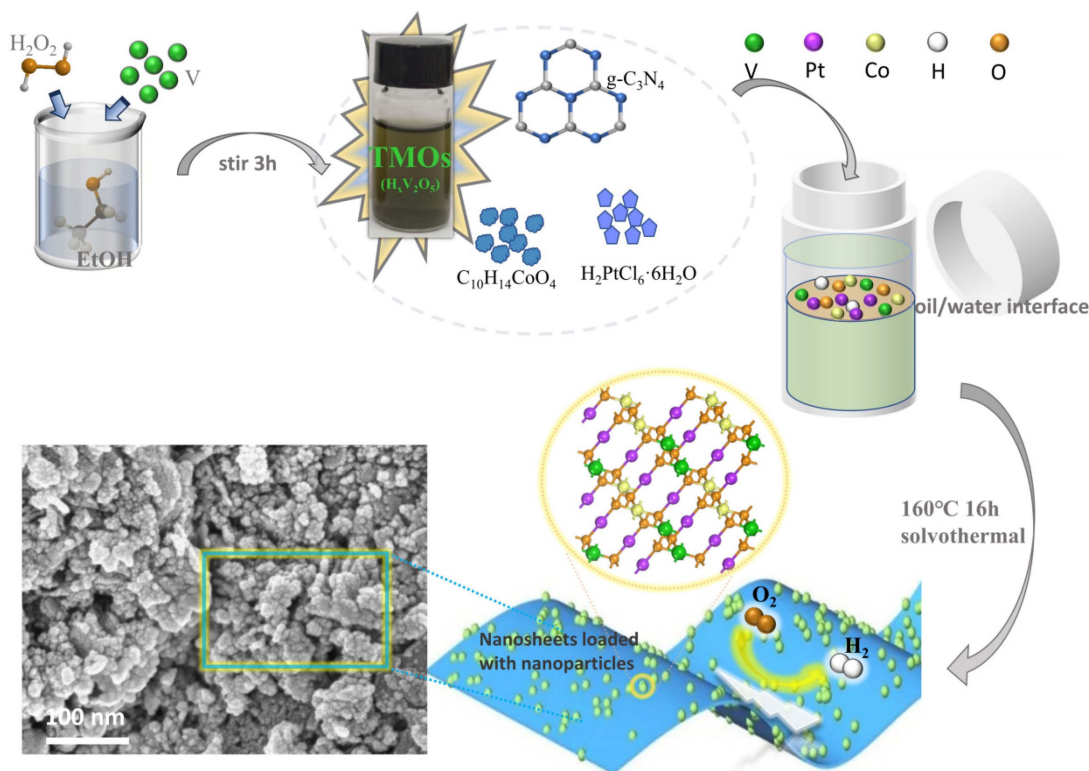


Figure 1. Schematic illustration of the synthesis process of PtCoVO/g-C₃N₄ nanocomposites at the oil/water interface.

2.2. Electrocatalytic Enhancement Mechanism

In order to thoroughly investigate the mechanism behind the hydrogen evolution reaction (HER) enhancement and the improved properties of PtCoVO/g-C₃N₄, the crystal structures of PtCo/g-C₃N₄ and PtCoVO/g-C₃N₄ (illustration of Figure 2a) were constructed [23]. Owing to having the identical supporter on two-dimensional g-C₃N₄ nanosheets, we focused on PtCo and PtCoVO for simplified models. DFT studies were executed to survey the effect of PtCo and PtCoVO on the atomic-level electronic structure [24]. A potential electrocatalyst is characterized by favorable hydrogen adsorption free energy (ΔG_{H^*}), where a ΔG_{H^*} value close to zero can lead to enhanced hydrogen evolution activity due to an optimal equilibrium between the absorption and desorption of hydrogen atoms from the active site. The PtCo free energy change (ΔG_{H^*}) in the hydrogen adsorption value deviates significantly from the optimal value (≈ 0 eV) [25], that is, the PtCo surface is inactive in Figure 2a. However, the ΔG_{H^*} value of PtCoVO combined with an H atom with HMOs (hydrogen metal oxide bronzes) is much smaller, 0.18 eV, which is conducive to the hydrogen evolution reaction [26]. The structure diagram of PtCo (H^{*}) and PtCoVO (H^{*}) is shown in Figures S2 and S3. Likewise, the density of states (DOS) analysis demonstrates that the PtCoVO catalyst exhibits a significantly higher density of states in close proximity to the Fermi level compared to the other substrates [27], when compared with PtCo/g-C₃N₄ (Figure 2b,c). When $H_xV_2O_5$ (HMOs) is added to frame, the DOS of PtCoVO is much higher than that PtCo, which indicates that the implanting of $H_xV_2O_5$ significantly enhances the DOS. This indicates that V is the active site in PtCoVO. The high DOS indicates increased electron transfer, thereby accelerating the electrocatalytic reaction and resulting in a significant improvement in HER performance [28]. Figures S4–S9 also verify this conclusion.

Additionally, the intensity of the DOS is strongly correlated with the conductivity [29]. The enhanced charge transfer dynamics of PtCoVO can be attributed to its higher DOS intensity, which aligns with the reduced charge transfer resistance. In addition, we can derive data from Figure S10 showing that the DOS of V in PtCoVO at the Fermi level is 2.511 eV, which is much higher than the DOS of PtCo, but close to that of PtCoVO. Therefore, we can ascertain that the introduction of V improves the DOS. The catalytic activity is closely related to the catalyst surface free energy of the hydrogen adsorption [30]. Moreover, the charge density difference model of PtCo and PtCoVO is depicted in Figure 2d,e. The charge density distribution of PtCo and PtCoVO indicate that doping with V atoms exacerbates the inhomogeneity of the distribution of electric charge. The HER activity of the catalyst is thus increased, so doping with V can introduce a large number of active catalytic sites, which has a crucial advantage for the successful release of hydrogen [31,32]. In addition, we also plot the molecular models of PtCoV and PtCoV (*), the band structure, and the PDOS (partial density of states), which can be shown in Figures S11–S14.

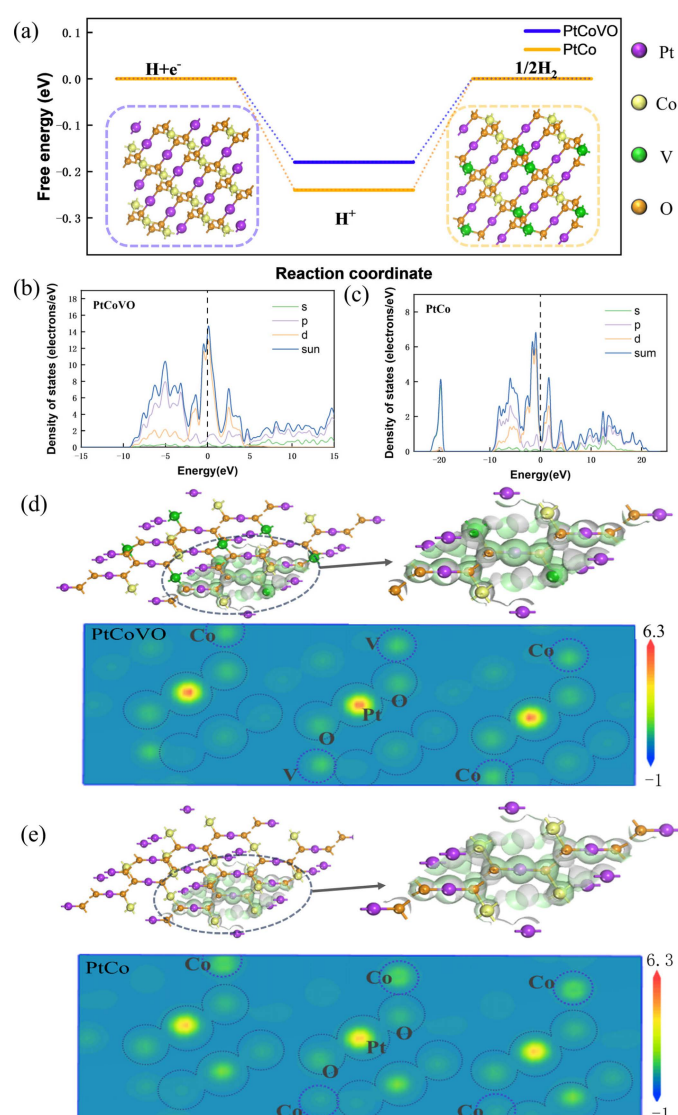


Figure 2. (a) Free energy diagrams for the HER of PtCo and PtCoVO. The diagram depicts the molecular structure of PtCo and PtCoVO. (b,c) The calculated DOS of PtCoVO and PtCo. (d,e) The charge density distribution of PtCoVO and PtCo.

Figure 3a illustrates the scanning electron microscopy (SEM) image of the as-synthesized trimetallic PtCoVO nanoparticles decorated onto the g-C₃N₄ nanosheets. The correspond-

ing energy dispersive X-ray (EDX) spectrum confirmed the uniform distribution of Co, Pt, V, C, N, and O atoms throughout the material (Figures S15 and S16). It appeared that Pt, Co, V, C, N, and O existed in PtCoVO/g-C₃N₄. Weight (Wt) ratios of PtCoVO/g-C₃N₄ elements were measured by EDX analysis. The Wt ratio of each element in the PtCoVO/g-C₃N₄ was 26.80:13.86:21.50:9.08:9.56:20.20 (C:N:O:Pt:Co:V). The precise mass ratio of each element in PtCoVO/g-C₃N₄ was determined using inductively coupled plasma emission spectrometry (ICP-AES), which was 6.43:7.02:15.95 (Pt:Co:V), consistent with the mass ratio data measured by EDX (Table S1). The incorporation of the PtCoV nanoalloy into the g-C₃N₄ nanosheets was further confirmed by the high-resolution transmission electron microscopy (HRTEM) image shown in Figure 3b, which exhibits a lattice fringe spacing of 0.226 nm. This lattice was identified as the (111) crystallographic plane of Pt, according to the Powder Diffraction File (PDF#04-0802) [33]. Meanwhile, structural information could be extracted by analyzing the fast Fourier transform (FFT) and inverse fast Fourier transform (IFFT) modes of the selected region for details of the structure [34] (Figure 3c,d). The lattice stripes observed in Figure 3e, Selected Area Electron Diffraction (SAED) images, indicate that they originated from the (111) and (200) crystallographic planes of Pt, as identified by the (PDF#04-0802). The FFT images shown in Figure 3f provide additional confirmation of the lattice spacing of approximately 2.265 nm (equivalent to 10 lattice distances) between the atomic layers of the exposed (111) facet. The use of High Angle Annular Dark Field Scanning Transmission Electron Microscopy (HAADF-STEM) confirmed the spatial distribution of various elements within the nanocomposite. The representative TEM EDS elemental mapping analysis depicted in Figure 3g demonstrates the uniform distribution of Pt, Co, V, C, N, and O elements throughout the structure [35], respectively. TEM image characterization of PtCoV/g-C₃N₄ is shown in Figures S17 and S18. The crystal structure of the materials was examined using X-ray diffraction (XRD) analysis, as represented in Figure 3h. The peaks of 39.76°, 46.24°, and 67.46° belong to the (111), (200), and (220) crystal faces of Pt (PDF#04-0802), respectively [36]. For PtCoVO/g-C₃N₄, the diffraction peak of g-C₃N₄ can be observed, which fully indicates that PtCoVO and g-C₃N₄ are formed between chemical bonds. In the XRD pattern, there were fewer diffraction peaks associated with Pt, which might be caused by the low content of Pt. Electron paramagnetic resonance (EPR) is a shortcut and highly sensitive technique for monitoring the presence of oxygen vacancies [37]. PtCoVO/g-C₃N₄ exhibited a greater EPR signal strength at $g = 1.97$ ($g = hv/\beta H$) than PtCo-C₃N₄ (Figure 3i). The superior value of g can be attributed to oxygen vacancies on the catalytic material surfaces [38], which indicates the existence of surface oxygen vacancies on PtCoVO/g-C₃N₄.

In order to investigate the alterations in the electronic structure and elemental valence of PtCoVO/g-C₃N₄ and PtCoV/g-C₃N₄, X-ray photoelectron spectroscopy (XPS) analysis was conducted. The findings are presented in Figure 4a–d. The full XPS spectrum indicates the presence of Co, Pt, V, O, C, and N elements in the PtCoVO/g-C₃N₄ and PtCoV/g-C₃N₄ samples, corroborating the results obtained from the EDS analysis [39]. Figure 4a illustrates the XPS analysis of PtCoVO/g-C₃N₄, revealing two prominent peaks at 71.4 eV and 74.88 eV, which correspond to metallic Pt 4f_{7/2} and 4f_{5/2}, respectively. Additionally, the presence of other peaks at 71.9 eV and 75.3 eV in the PtCoVO/g-C₃N₄ spectrum confirms the existence of oxidized states of Pt [40]. Compared to PtCoV/g-C₃N₄, the binding energy of PtCoVO/g-C₃N₄ displays a minor negative shift, which is related to the charge density change in the core metal ions [41]. In the case of V 2p, the peaks observed at binding energies of 521.23 eV and 525.18 eV in the PtCoVO/g-C₃N₄ spectrum (Figure 4b) can be assigned to V 2p_{1/2} and V 2p_{3/2} peaks, while a peak at 517.48 eV corresponds to V 2p_{3/2} in PtCoVO/g-C₃N₄, respectively [42]. In Figure 4c, the Co 2p spectra of PtCoVO/g-C₃N₄ exhibit two prominent peaks at 781.7 eV and 796.8 eV, corresponding to Co 2p_{3/2} and Co 2p_{1/2}, respectively. Additionally, two shakeup satellite peaks (labeled as Sat.) are observed in the Co 2p spectra of PtCoVO/g-C₃N₄, located at 786.9 eV and 803.1 eV, indicating characteristic peaks associated with Co²⁺ species [43]. It can be observed that there is a peak at 781.7 eV in PtCoVO/g-C₃N₄ that can be designated as a Co-N bond. To further}}

explain the existence of this Co-N bond, we tested the N 1s XPS spectra of PtCoVO/g-C₃N₄ (Figure S19), which were divided into 399.6 and 400.7 eV for g-C₃N₄, corresponding to Co-N and graphite N, respectively [44]. Figure 4d presents the high-resolution spectrum of O 1s. In the PtCoVO/g-C₃N₄ spectrum, the binding energy of the M-OH bond is measured to be 530.9 eV [45]. In comparison to PtCoV/g-C₃N₄, PtCoVO/g-C₃N₄ exhibits a minor shift in the O 1s peak, with a forward shift of 0.5 eV for one sample and a negative shift of 0.6 eV for another sample. This observation suggests that the variation in vanadium species in PtCoVO/g-C₃N₄ resulted in an increased number of active sites, potentially altering electron transfer processes and enhancing the catalytic performance of PtCoVO/g-C₃N₄.

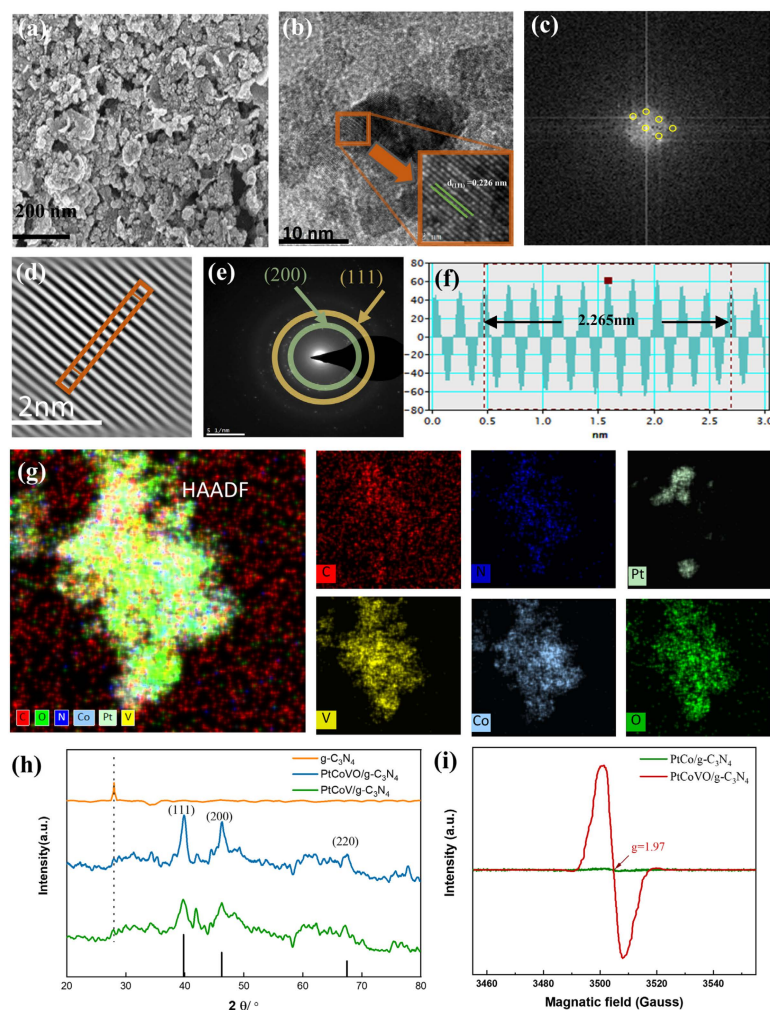


Figure 3. (a) SEM images of PtCoVO/g-C₃N₄. (b) TEM images of PtCoVO/g-C₃N₄. (c,d) FFT and IFFT pattern of PtCoVO/g-C₃N₄. (e) SAED images of PtCoVO/g-C₃N₄. (f) The PtCoVO/g-C₃N₄ spacing was 0.2265 nm. (g) HAADF of PtCoVO/g-C₃N₄ and elemental mapping of C, N, Pt, V, Co, and O, respectively. (h) XRD of PtCoVO/g-C₃N₄ and PtCoV/g-C₃N₄, standard card (PDF#04-0802). (i) EPR spectra of PtCoV/g-C₃N₄ and PtCoVO/g-C₃N₄ at 103 K in liquid N₂.

Ultraviolet photoelectron spectroscopy (UPS) was employed to examine the energy band structures of the synthesized H_xV₂O₅, PtCoVO/g-C₃N₄, and PtCoV/g-C₃N₄ samples [46]. As depicted in Figure 4e, the UPS results reveal a strong correlation between the doping of Pt and Co metals and the secondary electronic cutoff edge of the catalytic materials [47]. The work function (W_F) of a semiconductor is the difference between the Fermi level (E_F) and the energy level E_0 of the electron at rest in a vacuum [48,49]. The W_F of a material is typically around half the ionization energy of its corresponding metal-free atom. The W_F can be computed using the formula provided in Note S1 [50]. The magnitude

of the W_F reflects the strength of electron binding within the metal. A smaller W_F indicates that electrons are more likely to be released from the metal [51]. Pt possesses the highest W_F of 5.65 eV. This high work function is advantageous in demonstrating the ease with which catalytic materials can be prepared by electronic means, resulting in superior electrochemical catalytic performance. As calculated from the UPS results, the PtCoVO/g- C_3N_4 presents an E_F of 9.37 eV [52,53]. Compared with PtCo/g- C_3N_4 ($W_F = 5.2$ eV) and PtCoV/g- C_3N_4 ($W_F = 4.83$ eV), PtCoVO/g- C_3N_4 has the lowest $W_F = 4.42$ eV. By examining the slope of the VB-XPS curve displayed in Figure 4f, we can observe the valence band maximum (VBM), denoted as EVB, of different materials. Specifically, $H_xV_2O_5$, PtCo/g- C_3N_4 , and PtCoVO/g- C_3N_4 have EVB values of 1.48 eV, -0.48 eV, and -1.20 eV, respectively. These data suggest that PtCoVO/g- C_3N_4 exhibits the most negative EVB value among the three materials, resulting in a higher Schottky barrier at the metal/interface for charge transport. Figures S20 and S21 display the UPS spectra of PtCoVO/g- C_3N_4 at various levels of g- C_3N_4 added, alongside the VB-XPS spectrum.

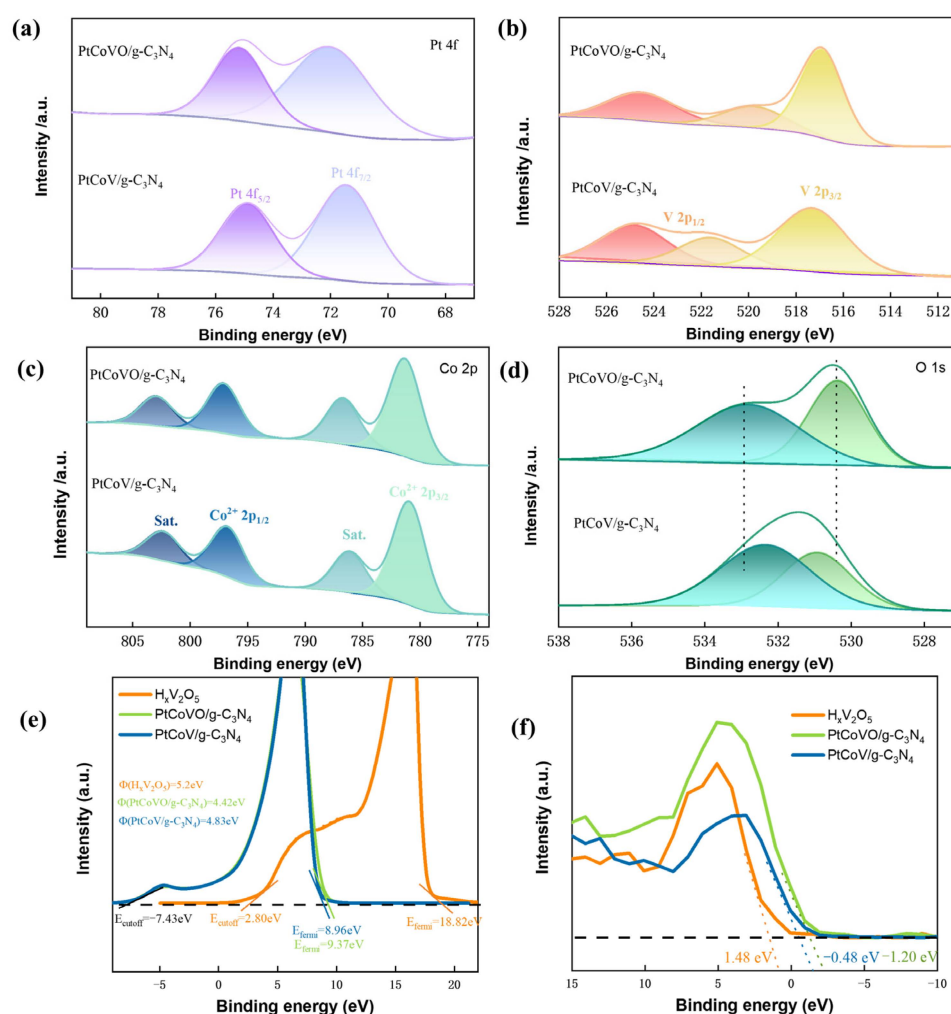


Figure 4. XPS spectra of PtCoVO/g- C_3N_4 and PtCoV/g- C_3N_4 . (a) Pt 4f. (b) V 2p. (c) Co 2p. (d) O 1s. (e) UPS spectra of $H_xV_2O_5$, PtCoVO/g- C_3N_4 , and PtCoV/g- C_3N_4 . (f) VB-XPS valence band spectra of $H_xV_2O_5$, PtCoVO/g- C_3N_4 , and PtCoV/g- C_3N_4 .

2.3. HER Electrocatalytic Performance Analyses

To assess the electrocatalytic characteristics of the prepared materials, the HER properties were examined using a conventional three-electrode system in a 1 M potassium hydroxide solution. This evaluation aimed to gain insights into the electrocatalytic performance of the polymetallic-doped materials. To facilitate comparison, a commercially

available Pt/C 20% catalyst was utilized as a reference. To ensure consistency, all potentials were calibrated with respect to the reversible hydrogen electrode (RHE). This standardization allows for accurate and meaningful comparisons between the different catalysts. According to the polarization curves plotted in Figure 5a, Pt/C 20% has the lowest overpotential of $\eta_{10} = 90.6$ mV to drive a current density of 10 mA cm^{-2} , as expected [54,55]; contrarily, the bimetallic material (PtCo/g-C₃N₄) demonstrates a higher overpotential, specifically $\eta_{10} = 386$ mV, which indicates poor activity in comparison. In our this work, all trimetallic catalysts performed better than bimetallic materials. The catalytic performance of PtCoVO/g-C₃N₄ was found to be exceptional, as evidenced by its significantly lower overpotential of $\eta_{10} = 92$ mV when compared to that of PtCoV/g-C₃N₄ ($\eta_{10} = 346$ mV). This remarkable improvement of 254 mV highlights the superior activity of PtCoVO/g-C₃N₄ as a catalyst.

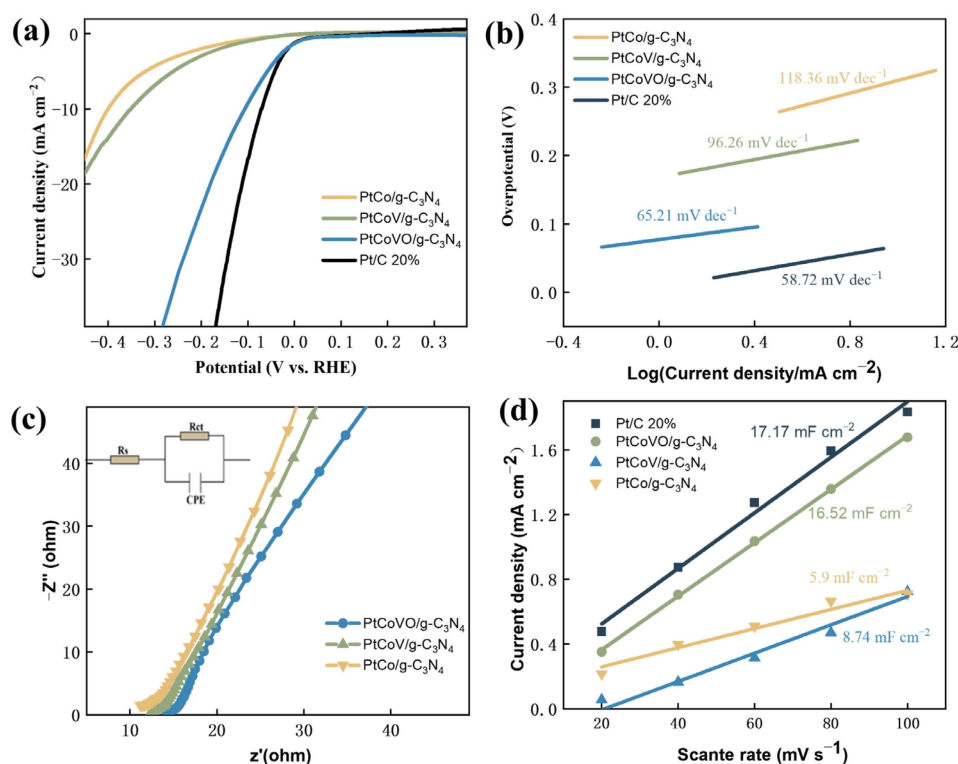


Figure 5. (a) HER polarization curves. (b) Tafel plots of PtCo/g-C₃N₄, Pt/C 20%, PtCoVO/g-C₃N₄, and PtCoV/g-C₃N₄. (c) EIS Nyquist plots of PtCoVO/g-C₃N₄, PtCo/g-C₃N₄, and PtCoV/g-C₃N₄. (d) C_{dl} values of current density differences plotted against scan rates of Pt/C 20%, PtCoVO/g-C₃N₄, PtCo/g-C₃N₄, and PtCoV/g-C₃N₄.

However, this difference in activity between PtCoVO/g-C₃N₄ and PtCoV/g-C₃N₄ could be a result of the higher catalyst activity due to the insertion of H_xV₂O₅ (Figure 5a). This result was further confirmed by the optimization of the PtCoVO/g-C₃N₄ element ratio as the HER activity exhibited an upward trend with increasing H_xV₂O₅ content. Notably, the HER activity reached its maximum when the ratio of Pt:Co:V was 0.1:0.4:0.4 (Figure S22). In addition, we also explored the polarization curves of Pt prepared by adding vanadium powder in different proportions (Figure S23), which also confirmed that the overpotential is the lowest at a ratio from 0.1 to 0.4. Thus, the PtCo/g-C₃N₄ and PtCoV/g-C₃N₄ used for comparison were prepared in this ratio. The catalytic mechanism of the HER can also be revealed by Tafel plots [56,57]. In general, there are three classical reactions for H₂ evolution: electrochemical hydrogen ion adsorption (Volmer reaction), chemical desorption (Tafel reaction), and electrochemical desorption (Heyrovsky reaction) [58,59]. The first step in the HER is always the Volmer reaction, but the next step is either the Heyrovsky reaction or the Tafel reaction [60]. The calculated Tafel slopes of all samples are given in

Figure 5b. The PtCoVO/g-C₃N₄ material displays the smallest Tafel slope (65.21 mV dec⁻¹) among all tested materials, excluding Pt/C 20%. This result confirms the faster kinetics of the PtCoVO/g-C₃N₄ catalyst, indicating its superior performance in facilitating the hydrogen evolution reaction. However, PtCoVO/g-C₃N₄ exhibits a lower Tafel slope, thus demonstrating a much faster and efficient process of the HER compared to other compositions [61]. The verification of this result is supported by the comparison of performance, Tafel slopes, and overpotentials of the PtCoVO/g-C₃N₄ catalyst with some previously reported electrocatalytic materials, as shown in Table S2. This comparison further confirms the superior performance and efficiency of PtCoVO/g-C₃N₄ in catalyzing the desired electrochemical reactions. Zhang et al. reported the good synergy between NiCo₂O₄ and C₃N₄, as many electrons tend to transfer from the hydrophobic region (NiCo₂O₄) to the electrophilic region (C₃N₄) and then to water, resulting in electron accumulation in water. DFT calculations shows that the E_{H₂O*} and ΔG_{H*} of NiCo₂O₄@C₃N₄ are decreased [62]. In the study of Lu, the formed C₃N₄ layer with a large degree of graphitization can not only improve the conductivity of the catalyst, but can also prevent the corrosion of the active tungsten dioxide nanorods during the HER, exerting a protective effect [63]. Zhao et al. reported that CuSCN/C₃N₄ exhibited an overpotential of 85 mV, which is much higher than that of pure CuSCN. An interfacial N-Cu-S coordination mode is formed, which can promote electron penetration from the CuSCN crystal into the N atoms of the C₃N₄ shell, thereby improving the HER reactivity [64]. This indicates that these materials have a good synergistic effect with C₃N₄ (Table S3). By adjusting the surface structure of transition metal atoms, reasonable design can obtain low-cost and efficient electrocatalysts, which is the key to developing an electrocatalytic HER.

The Nyquist diagram, depicted in Figure 5c, was obtained through electrochemical impedance spectroscopy (EIS) measurements. The measured data align closely with the equivalent circuit model comprising charge transfer resistance (R_{ct}), solution resistance (R_s), and a constant phase element (CPE), as illustrated in the insert of Figure 5c. The EIS results revealed that the R_{ct} of the PtCoVO/g-C₃N₄ catalyst was significantly lower in the lower frequency region compared to that of PtCo/g-C₃N₄ and PtCoV/g-C₃N₄. This indicates that PtCoVO/g-C₃N₄ exhibited the highest electronic conductivity for the HER process, facilitating the fastest charge transfer rate and displaying the most sensitive electrocatalytic kinetics. Therefore, the resistance obtained from the EIS spectra of various materials shows that the PtCoVO/g-C₃N₄ catalyst has obvious lower impedance, which explains that the PtCoVO/g-C₃N₄ catalyst has faster reaction kinetics than the PtCo/g-C₃N₄ and PtCoV/g-C₃N₄ electrodes. In addition, the EIS spectra of different H_xV₂O₅ contents proved the minimum impedance at a millimolar ratio of 0.1:0.4:0.4, as shown in Figure S24. Moreover, the EIS measurements showed that PtCoVO/g-C₃N₄ possess the smallest electron transfer resistance (the charge transfer resistance decreases as the arc size decreases). The trend observed in EIS for solid solutions is generally consistent with the trend of HER activity [65,66].

The double-layer capacitance (C_{dl}) of PtCo/g-C₃N₄, PtCoVO/g-C₃N₄, and PtCoV/g-C₃N₄ was evaluated through cyclic voltammetry (CV) measurements performed at different scan rates ranging from 0.02 to 0.1 V [67]. Figures S25–S28 provide the electrochemical double-layer capacitance of various materials. Based on the resulting C_{dl} values depicted in Figure 5d, PtCoVO/g-C₃N₄ has the highest value of all samples; this finding further validates the enhanced performance of PtCoVO/g-C₃N₄. The electrochemically active surface area (ECSA) of PtCo/g-C₃N₄ (28.95 cm²), PtCoVO/g-C₃N₄ (81.05 cm²), and PtCoV/g-C₃N₄ (42.88 cm²) was estimated by the C_{dl}.

The XPS spectra shown in Figure 6a–d provide clear evidence that the PtCoVO/g-C₃N₄ material maintains excellent stability after undergoing electrocatalysis, providing a possible solution to the problem of durability in industrial applications. This statement can also be proved by the information in Figure S29. The chronoamperometry curve for PtCoVO/g-C₃N₄ demonstrates that the current density of PtCoVO/g-C₃N₄ is maintained at a constant value, with a minimal decrease observed only after 48 h of continuous operation, indicating

the exceptional long-term electrochemical stability of PtCoVO/g-C₃N₄ (Figure 6e) [68]. The TEM image, as shown in the inset of Figure 6e, confirms that the morphology of PtCoVO/g-C₃N₄ remained intact, with minimal changes. Furthermore, the long-term durability test of PtCoVO/g-C₃N₄ was evaluated by potential cycling in 1 M KOH. As shown in Figure 6f, no significant loss of activity occurred after 5000 cycles and the value remained overlapped with the previous data, highlighting the PtCoVO/g-C₃N₄ catalyst's excellent electrocatalytic stability [69]. The stability of the HER electrocatalyst properties of PtCoVO/g-C₃N₄ can be attributed to the notable influence of oxygen vacancies in H_xV₂O₅ on the electrical properties and optimized structural properties.

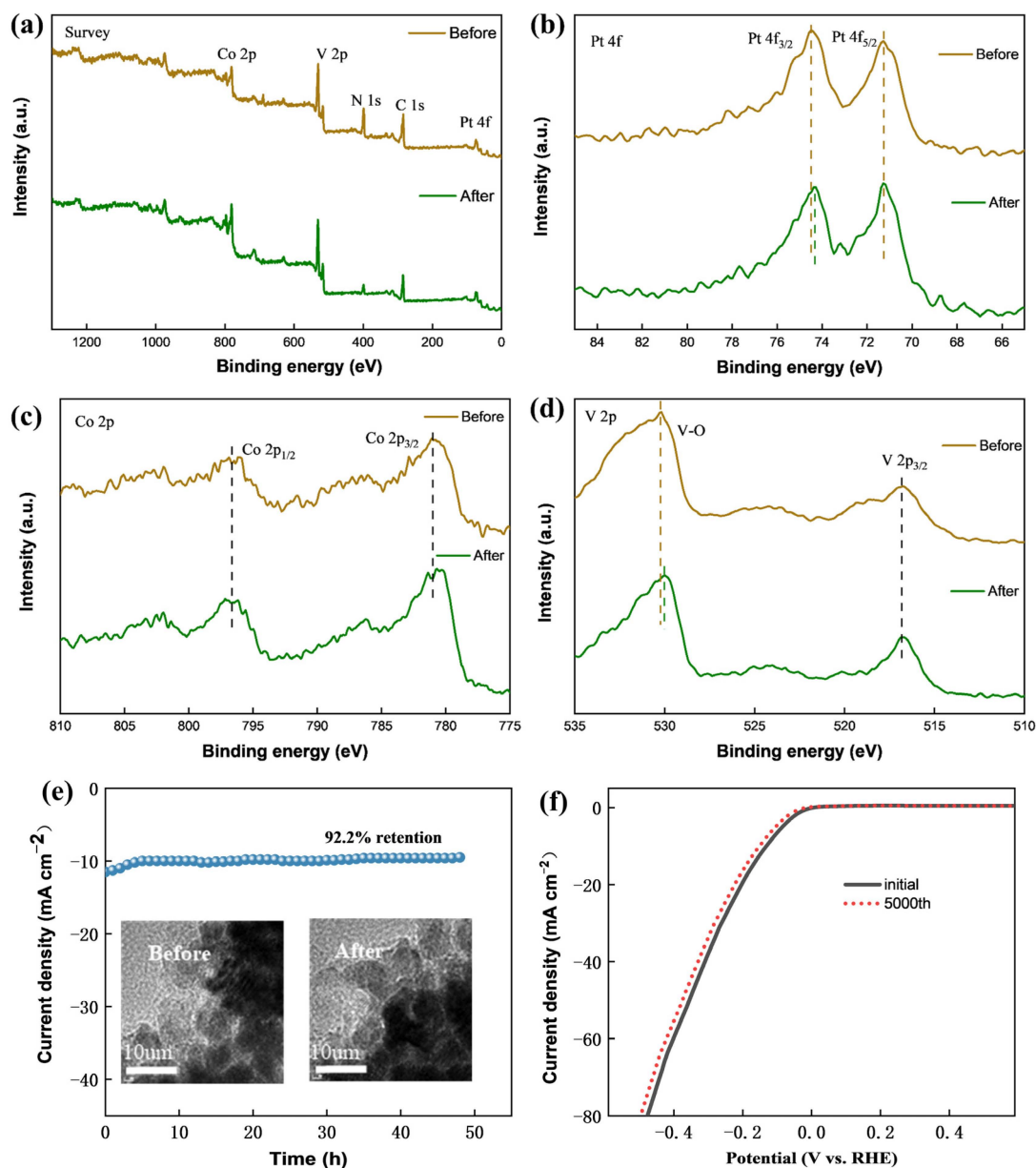


Figure 6. (a–d) XPS spectra of survey, Pt 4f, Co 2p, and V 2p for PtCoVO/g-C₃N₄ before and after electrochemical testing. (e) The PtCoVO/g-C₃N₄ catalyst was subjected to a long-term stability measurement at current densities of 10 mA cm⁻² for 48 h; the inset displays the TEM images before and after the stability measurement. (f) Continuous CV scanning after 5000 circles at 100 mV s⁻¹ of PtCoVO/g-C₃N₄.

3. Experimental Methods

3.1. Materials

Cobalt acetylacetonate ($C_{15}H_{21}CoO_6$, 98%), chloroplatinic acid hexahydrate ($H_2PtCl_6 \cdot 6H_2O$, 99%), oil amine ($C_{18}H_{37}N$, 90%), vanadium powder (V, 200 mesh, 99.999%), potassium hydroxide (KOH, 90%), absolute ethanol (EtOH, 99.7%), hydrogen peroxide (H_2O_2 , 30%), and urea (CH_4N_2O , 99%) were used. The materials mentioned above were acquired from Adamas Reagent. The Nafion solution (5wt.%, containing 15–20% water) was purchased from Sigma-Aldrich (Burlington, MA, USA). The aforementioned materials were utilized directly without undergoing any purification. The deionized water employed in the experiments was obtained by passing it through an ultrapure purification device.

3.2. Methods

3.2.1. Fabrication Process for g- C_3N_4 Nanosheets

Bulk g- C_3N_4 was prepared by the thermal treatment of urea. In the typical fabrication process, 5.0 g of urea was ground into a powder and subjected to calcination at 550 °C for 3 h, and the heating rate during this process was maintained at 5 °C/min. After cooling, a yellow solid was obtained and ground into powder for 30 min until the yellow color of g- C_3N_4 changed into a light-yellow color.

3.2.2. Synthesis of $H_xV_2O_5$ HMOs

Material Oxides Synthesis: A total of 0.5 g of vanadium powder was dispersed in 50 mL of ethanol; during the dispersion process, continuous stirring was maintained for several minutes. Next, the vanadium metal suspension solution was supplemented with 2.5 mL of H_2O_2 solution. Following a reaction period of 3 h, the vanadium oxide solution underwent a color change from orange to eventually brown. The solution was subsequently dried using a vacuum chamber and then ground for subsequent utilization.

3.2.3. Fabrication of PtCo/g- C_3N_4 , PtCoV/g- C_3N_4 , and PtCoVO/g- C_3N_4 Catalysts

(1) Preparation process for PtCo/g- C_3N_4 materials

In a conical flask, 10 mL of water, 5 mL of EtOH, and 2 mL of oil amine were added. Then, 40 mg of g- C_3N_4 , 142.5 mg of cobalt acetylacetonate, and 51.79 mg of chloroplatinic acid hexahydrate were weighed and introduced into the aforementioned solution. After subjecting the mixture to ultrasonic treatment for 60 min, it was transferred to a 25 mL reactor and maintained at 160 degrees Celsius for 16 h. The resulting solution was then allowed to cool naturally. When the temperature dropped down to room temperature, the product was obtained by centrifugation, washing, and drying. (Note: This material is named PtCo/g- C_3N_4 not because there is no oxygen element in the synthetic material, but in contrast with PtCoVO/g- C_3N_4 , the original material of this catalyst is vanadium powder, whereas the original material of PtCoVO/g- C_3N_4 is $H_xV_2O_5$, so the name distinguishes it. The same is true for PtCoV/g- C_3N_4).

(2) Preparation of PtCoVO/g- C_3N_4 materials

The preparation method for this material is similar to that of PtCo/g- C_3N_4 , with the addition of $H_xV_2O_5$.

(3) Preparation of PtCoV/g- C_3N_4 materials

The preparation method for this material is similar to that of PtCoVO/g- C_3N_4 , with the difference being that vanadium powder is used instead of $H_xV_2O_5$.

4. Conclusions

By controlling the reaction rate, hydrogen metal oxides bronzes (HMOs), namely, the hydrogen vanadium bronze ($H_xV_2O_5$), were obtained. Its oxygen content has a significant effect on its electrical properties. Subsequently, a novel hybrid nanocomposite consisting of g- C_3N_4 doped with a multi-metal was synthesized using a solvothermal method.

Compared with other catalysts, the obtained PtCoVO/g-C₃N₄ catalyst possesses the characteristics of close contact between non-metals and metals, remarkable activity, fast electron transport, easy release of bubbles generated, and exceptional electrocatalytic durability. This study of the design of high-efficiency catalysts for the HER provides a novel concept, detailing the theoretical analysis to guide the experiment and the experimental results to support the theoretical calculation, with the theory and experiment complementing each other. The present study introduces an efficient and robust catalyst for integrated catalysts, along with a scalable insertion preparation technique and design concept. These advancements open up possibilities for broader applications in the fields of electrocatalysis and material science.

Supplementary Materials: The following supporting information can be downloaded at: <https://www.mdpi.com/article/10.3390/molecules29071518/s1>. Refs. [63–65,70–83] are cited in Supplementary Materials.

Author Contributions: F.J. conceived the project and revised the manuscript. J.Z. synthesized the materials and analyzed the electrocatalytic performances. W.D. conducted the TEM results. Y.W. conducted the SEM results. J.J. analyzed the XPS data and the UPS data. H.M. conducted the electrocatalytic results. T.L. analyzed EPR data. D.L. conducted DFT calculations. W.Z. revised the XRD results. All authors have read and agreed to the published version of the manuscript.

Funding: This research received no external funding.

Institutional Review Board Statement: Not applicable.

Informed Consent Statement: Not applicable.

Data Availability Statement: Data are contained within the article and the Supplementary Materials.

Acknowledgments: F.J. and W.D. thank the computing resources staff in the super-computational center in the Shanghai Institute of Applied Physics, Chinese Academy of Sciences. The authors would like to thank Lingyu Wan from Shiyanjia Lab (www.shiyanjia.com) (accessed on 18 March 2024) for the TEM analysis.

Conflicts of Interest: The authors declare no conflicts of interest.

References

1. Seif, R.; Salem, F.Z.; Allam, N.K. E-waste recycled materials as efficient catalysts for renewable energy technologies and better environmental sustainability. *Environ. Dev. Sustain.* **2023**, *26*, 5473–5508. [[CrossRef](#)] [[PubMed](#)]
2. Deng, W.; Xie, W.S.; Li, D.; Gai, Y.P.; Chen, Z.D.; Yu, J.; Yang, R.Q.; Bao, X.C.; Jiang, F. Controllable tuning of polymetallic Co-Ni-Ru-S-Se ultrathin nanosheets to boost electrocatalytic oxygen evolution. *NPG Asia Mater.* **2022**, *14*, 25. [[CrossRef](#)]
3. Sangtani, R.; Nogueira, R.; Yadav, A.K.; Kiran, B. Systematizing Microbial Bioplastic Production for Developing Sustainable Bioeconomy: Metabolic Nexus Modeling, Economic and Environmental Technologies Assessment. *J. Polym. Environ.* **2023**, *31*, 2741–2760. [[CrossRef](#)] [[PubMed](#)]
4. Chen, J.; Chen, C.; Qin, M.; Li, B.; Lin, B.; Mao, Q.; Yang, H.; Liu, B.; Wang, Y. Reversible hydrogen spillover in Ru-WO_(3-x) enhances hydrogen evolution activity in neutral pH water splitting. *Nat. Commun.* **2022**, *13*, 5382. [[CrossRef](#)] [[PubMed](#)]
5. Jiang, F.; Choy, W.C.H.; Li, X.C.; Zhang, D.; Cheng, J.Q. Post-treatment-Free Solution-Processed Non-stoichiometric NiO_x Nanoparticles for Efficient Hole-Transport Layers of Organic Optoelectronic Devices. *Adv. Mater.* **2015**, *27*, 2930–2937. [[CrossRef](#)] [[PubMed](#)]
6. Hanan, A.; Lakhan, M.N.; Shu, D.; Hussain, A.; Ahmed, M.; Soomro, I.A.; Kumar, V.; Cao, D. An efficient and durable bifunctional electrocatalyst based on PdO and Co₂FeO₄ for HER and OER. *Int. J. Hydrogen Energy* **2023**, *48*, 19494–19508. [[CrossRef](#)]
7. Ganci, F.; Cusumano, V.; Livreri, P.; Aiello, G.; Sunseri, C.; Inguanta, R. Nanostructured Ni-Co alloy electrodes for both hydrogen and oxygen evolution reaction in alkaline electrolyzer. *Int. J. Hydrogen Energy* **2021**, *46*, 10082–10092. [[CrossRef](#)]
8. Saifi, S.; Dey, G.; Karthikeyan, J.; Sinha, A.S.K.; Aijaz, A. MoS₂ and WS₂ Nanosheets Decorated on Metal–Organic Framework-Derived Cobalt/Carbon Nanostructures as Electrocatalysts for Hydrogen Evolution. *ACS Appl. Nano Mater.* **2022**, *5*, 10696–10703. [[CrossRef](#)]
9. Zhang, B.; Zheng, Y.; Xing, Z.; Wu, Z.; Cheng, C.; Ma, T.; Li, S. Interfacial electron-engineered tungsten oxynitride interconnected rhodium layer for highly efficient all-pH-value hydrogen production. *J. Mater. Chem. A* **2024**, *12*, 4484–4491. [[CrossRef](#)]
10. Shen, H.; Liang, S.; Adimi, S.; Guo, X.; Zhu, Y.; Guo, H.; Thomas, T.; Attfield, J.P.; Yang, M. Supporting nickel on vanadium nitride for comparable hydrogen evolution performance to platinum in alkaline solution. *J. Mater. Chem. A* **2021**, *9*, 19669–19674. [[CrossRef](#)]

11. Zhang, L.; Lu, C.; Ye, F.; Pang, R.; Liu, Y.; Wu, Z.; Shao, Z.; Sun, Z.; Hu, L. Selenic Acid Etching Assisted Vacancy Engineering for Designing Highly Active Electrocatalysts toward the Oxygen Evolution Reaction. *Adv. Mater.* **2021**, *33*, 2007523. [[CrossRef](#)] [[PubMed](#)]
12. Baek, D.S.; Lee, J.; Kim, J.; Joo, S.H. Metastable Phase-Controlled Synthesis of Mesoporous Molybdenum Carbides for Efficient Alkaline Hydrogen Evolution. *ACS Catal.* **2022**, *12*, 7415–7426. [[CrossRef](#)]
13. Griesser, C.; Li, H.; Wernig, E.-M.; Winkler, D.; Nia, N.S.; Mairegger, T.; Götsch, T.; Schachinger, T.; Steiger-Thirsfeld, A.; Penner, S.; et al. True Nature of the Transition-Metal Carbide/Liquid Interface Determines Its Reactivity. *ACS Catal.* **2021**, *11*, 4920–4928. [[CrossRef](#)] [[PubMed](#)]
14. Tang, J.; Xu, X.; Tang, T.; Zhong, Y.; Shao, Z. Perovskite-based electrocatalysts for cost-effective ultrahigh-current-density water splitting in anion exchange membrane electrolyzer cell. *Small Methods* **2022**, *6*, 2201099. [[CrossRef](#)] [[PubMed](#)]
15. Fei, L.; Sun, H.; Xu, X.; Li, Y.; Ran, R.; Zhou, W.; Shao, Z. Understanding the bifunctional catalytic ability of electrocatalysts for oxygen evolution reaction and urea oxidation reaction: Recent advances and perspectives. *Chem. Eng. J.* **2023**, *471*, 144660. [[CrossRef](#)]
16. Abdelghafar, F.; Xu, X.; Shao, Z. Designing single-atom catalysts toward improved alkaline hydrogen evolution reaction. *Mater. Rep. Energy* **2022**, *2*, 100144. [[CrossRef](#)]
17. Lei, H.; Wan, Q.; Tan, S.; Wang, Z.; Mai, W. Pt-Quantum-Dot-Modified Sulfur-Doped NiFe Layered Double Hydroxide for High-Current-Density Alkaline Water Splitting at Industrial Temperature. *Adv. Mater.* **2023**, *35*, 2208209. [[CrossRef](#)] [[PubMed](#)]
18. Lu, Y.; Huang, K.; Cao, X.; Zhang, L.; Wang, T.; Peng, D.; Zhang, B.; Liu, Z.; Wu, J.; Zhang, Y.; et al. Atomically Dispersed Intrinsic Hollow Sites of M-M₁-M (M₁ = Pt, Ir; M = Fe, Co, Ni, Cu, Pt, Ir) on FeCoNiCuPtIr Nanocrystals Enabling Rapid Water Redox. *Adv. Funct. Mater.* **2022**, *32*, 2110645. [[CrossRef](#)]
19. Zhang, J.; Wang, M.; Wan, T.; Shi, H.; Lv, A.; Xiao, W.; Jiao, S. Novel (Pt-O_x)-(Co-O_y) Nonbonding Active Structures on Defective Carbon from Oxygen-Rich Coal Tar Pitch for Efficient HER and ORR. *Adv. Mater.* **2022**, *34*, e2206960. [[CrossRef](#)] [[PubMed](#)]
20. Zhong, P.; Wang, K.; Wang, X.; Lu, Z.; Xie, J.; Cao, Y. Hollow porous nitrogen-doped carbon embedded with ultrafine Co nanoparticles boosting lithium-ion storage. *CrystEngComm* **2021**, *23*, 2006–2015. [[CrossRef](#)]
21. Xie, F.; Choy, W.C.; Wang, C.; Li, X.; Zhang, S.; Hou, J. Low-temperature solution-processed hydrogen molybdenum and vanadium bronzes for an efficient hole-transport layer in organic electronics. *Adv. Mater.* **2013**, *25*, 2051–2055. [[CrossRef](#)] [[PubMed](#)]
22. Zhang, J.; Deng, W.; Weng, Y.; Li, X.; Mao, H.; Zhang, W.; Lu, T.; Long, D.; Jiang, F. Theoretical Revelation and Experimental Verification Synergistic Electronic Interaction of V-Doped RuNi as an Efficient Bifunctional Electrocatalyst for Overall Water Splitting. *ACS Sustain. Chem. Eng.* **2023**, *11*, 16288–16299. [[CrossRef](#)]
23. Shinde, P.V.; Mane, P.; Chakraborty, B.; Rout, C.S. Spinel NiFe₂O₄ nanoparticles decorated 2D Ti₃C₂ MXene sheets for efficient water splitting: Experiments and theories. *J. Colloid Interface Sci.* **2021**, *602*, 232–241. [[CrossRef](#)] [[PubMed](#)]
24. Zhao, Y.; Wang, X.; Li, Z.; Zhao, P.; Tao, C.; Cheng, G.; Luo, W. Enhanced catalytic activity of Ru through N modification toward alkaline hydrogen electrocatalysis. *Chin. Chem. Lett.* **2022**, *33*, 1065–1069. [[CrossRef](#)]
25. Hussain, S.; Vikraman, D.; Truong, L.; Akbar, K.; Rabani, I.; Kim, H.-S.; Chun, S.-H.; Jung, J. Facile and cost-effective growth of MoS₂ on 3D porous graphene-coated Ni foam for robust and stable hydrogen evolution reaction. *J. Alloys Compd.* **2019**, *788*, 267–276. [[CrossRef](#)]
26. Zhang, Z.; Liu, H.; Ni, L.; Zhao, Z.L.; Li, H. Scalable synthesis of hcp ruthenium-molybdenum nanoalloy as a robust bifunctional electrocatalyst for hydrogen evolution/oxidation. *J. Energy Chem.* **2022**, *72*, 176–185. [[CrossRef](#)]
27. Li, X.; Deng, W.; Weng, Y.; Zhang, J.; Mao, H.; Zhang, W.; Lu, T.; Long, D.; Jiang, F. Controllable tuning graphene composited PtCoYOx nanocomposites to promote electrocatalytic hydrogen evolution. *Appl. Catal. A Gen.* **2023**, *665*, 119359. [[CrossRef](#)]
28. Martínez-Alonso, C.; Guevara-Vela, J.M.; Llorca, J. The effect of elastic strains on the adsorption energy of H, O, and OH in transition metals. *Phys. Chem. Chem. Phys.* **2021**, *23*, 21295–21306. [[CrossRef](#)] [[PubMed](#)]
29. Liu, D.; Chen, M.; An, K.; Liu, D.; Chen, Y.; Zhou, P.; Li, J.; Feng, J.; Ke, Y.; Liu, D.; et al. In situ surface reconstruction on LaCoO₃-δ leads to enhanced hydrogen evolution reaction. *J. Alloys Compd.* **2022**, *891*, 161754. [[CrossRef](#)]
30. Su, X.; Meng, F.; Tan, H.; Chen, G. Unravelling the CO₂ methanation mechanisms on a Ni-BaTiO₃ catalyst: A theoretical investigation. *J. CO₂ Util.* **2022**, *64*, 102170. [[CrossRef](#)]
31. Zhang, P.; Li, Y.; Zhang, Y.; Hou, R.; Zhang, X.; Xue, C.; Wang, S.; Zhu, B.; Li, N.; Shao, G. Photogenerated electron transfer process in heterojunctions: In situ irradiation XPS. *Small Methods* **2020**, *4*, 2000214. [[CrossRef](#)]
32. Du, J.; Qin, Y.; Dou, T.; Ge, J.; Wang, Y.; Zhao, X.; Zhang, F.; Lei, X. Copper Nanoparticles Dotted on Copper Sulfide Nanosheets for Selective Electrocatalytic Oxidation of Glycerol to Formate. *ACS Appl. Nano Mater.* **2022**, *5*, 10174–10182. [[CrossRef](#)]
33. Dawn, R.; Zzaman, M.; Faizal, F.; Kiran, C.; Kumari, A.; Shahid, R.; Panatarani, C.; Joni, I.M.; Verma, V.K.; Sahoo, S.K.; et al. Origin of Magnetization in Silica-coated Fe₃O₄ Nanoparticles Revealed by Soft X-ray Magnetic Circular Dichroism. *Braz. J. Phys.* **2022**, *52*, 99. [[CrossRef](#)]
34. Li, X.; Deng, W.; Weng, Y.; Zhang, J.; Mao, H.; Lu, T.; Zhang, W.; Yang, R.; Jiang, F. Implanting H_xYO_{2-x} sites into Ru-doped graphene and oxygen vacancies for low-overpotential alkaline hydrogen evolution. *NPG Asia Mater.* **2023**, *15*, 55. [[CrossRef](#)]
35. Kitta, M.; Taguchi, N.; Sudrajat, H.; Onishi, H. Direct confirmation of the dopant site in indium-doped SrTiO₃ photocatalyst via atomic-scale analytical transmission electron microscopy imaging. *Appl. Phys. Lett.* **2021**, *118*, 153901. [[CrossRef](#)]

36. Zheng, H.-B.; Li, Y.-L.; Wang, Y.-L.; Ma, F.; Gao, P.-Z.; Guo, W.-M.; Qin, H.; Liu, X.-P.; Xiao, H.-N. Fabrication of $\text{Co}(\text{PO}_3)_2@\text{NPC}/\text{MoS}_2$ heterostructures for enhanced electrocatalytic hydrogen evolution. *J. Alloys Compd.* **2022**, *894*, 162411. [[CrossRef](#)]
37. Wei, Z.; Liu, Y.; Zong, R.; Yao, W.; Wang, J.; Zhu, Y. Controlled synthesis of a highly dispersed BiPO_4 photocatalyst with surface oxygen vacancies. *Nanoscale* **2015**, *7*, 13943–13950. [[CrossRef](#)]
38. Li, J.-J.; Weng, B.; Cai, S.-C.; Chen, J.; Jia, H.-P.; Xu, Y.-J. Efficient promotion of charge transfer and separation in hydrogenated TiO_2/WO_3 with rich surface-oxygen-vacancies for photodecomposition of gaseous toluene. *J. Hazard. Mater.* **2018**, *342*, 661–669. [[CrossRef](#)] [[PubMed](#)]
39. Besley, N.A. Density functional theory based methods for the calculation of X-ray spectroscopy. *Acc. Chem. Res.* **2020**, *53*, 1306–1315. [[CrossRef](#)]
40. Baronia, R.; Goel, J.; Tiwari, S.; Singh, P.; Singh, D.; Singh, S.P.; Singhal, S.K. Efficient electro-oxidation of methanol using PtCo nanocatalysts supported reduced graphene oxide matrix as anode for DMFC. *Int. J. Hydrogen Energy* **2017**, *42*, 10238–10247. [[CrossRef](#)]
41. Yi, M.; Hu, S.; Lu, B.; Li, N.; Zhu, Z.; Huang, X.; Wang, M.; Zhang, J. Multicomponent Pt/PtTe₂/NiCoTe₂ embedded in ternary heteroatoms-doped carbon for efficient and pH-universal hydrogen evolution reaction. *J. Alloys Compd.* **2021**, *884*, 161042. [[CrossRef](#)]
42. Zhang, J.; Deng, W.; Weng, Y.; Li, X.; Mao, H.; Lu, T.; Zhang, W.; Long, D.; Jiang, F. Experimentally revealed and theoretically certified synergistic electronic interaction of V-doped CoS for facilitating the oxygen evolution reaction. *Phys. Chem. Chem. Phys.* **2023**, *25*, 21661–21672. [[CrossRef](#)] [[PubMed](#)]
43. Deng, W.; Gai, Y.; Li, D.; Chen, Z.; Xie, W.; Yu, J.; Yang, R.; Bao, X.; Jiang, F. Bifunctional doped transition metal CoSSeNi–Pt/C for efficient electrochemical water splitting. *Int. J. Hydrogen Energy* **2022**, *47*, 16862–16872. [[CrossRef](#)]
44. Chen, Z.; Deng, W.; Li, D.; Gai, Y.; Xie, W.; Hu, X.; Han, S.; Xu, N.; Qiao, S.; Yu, J.; et al. Construction of CoNiSSe-g-C₃N₄ nanosheets with high exposed conductive interface for boosting oxygen evolution reaction. *J. Alloys Compd.* **2021**, *887*, 161346. [[CrossRef](#)]
45. Zhao, P.; Yin, T.; Doi, T.; Kurokawa, S.; Seshimo, K.; Ye, D.; Cai, J. Effect of Mn-Based Slurries on Chemical Mechanical Polishing of SiC Substrates. *ECS J. Solid State Sci. Technol.* **2022**, *11*, 074002. [[CrossRef](#)]
46. Béchu, S.; Ralaizarisoa, M.; Etcheberry, A.; Schulz, P. Photoemission spectroscopy characterization of halide perovskites. *Adv. Energy Mater.* **2020**, *10*, 1904007. [[CrossRef](#)]
47. Wang, Q.; Yu, R.; Shen, D.; Liu, Q.; Luo, K.H.; Wu, C.; Gu, S. Performance of intrinsic heteroatoms in cobalt phosphide loaded ginkgo leaf-based carbon material on promoting the electrocatalytic activity during hydrogen evolution reaction and oxygen evolution reaction. *Fuel* **2023**, *333*, 126368. [[CrossRef](#)]
48. Alli, Y.A.; Oladoye, P.O.; Ejeromedoghene, O.; Bankole, O.M.; Alimi, O.A.; Omotola, E.O.; Olanrewaju, C.A.; Philippot, K.; Adeleye, A.S.; Ogunlaja, A.S. Nanomaterials as catalysts for CO₂ transformation into value-added products: A review. *Sci. Total Environ.* **2023**, *868*, 161547. [[CrossRef](#)] [[PubMed](#)]
49. Reynosa-Martínez, A.C.; Gómez-Chayres, E.; Villaurrutia, R.; López-Honorato, E. Controlled reduction of graphene oxide using sulfuric acid. *Materials* **2020**, *14*, 59. [[CrossRef](#)]
50. Kumar, P.S.; Prakash, P. Metal free nanocomposite of graphitic carbon nitride, boron nitride and chitosan for efficient evolution of hydrogen: A strategic approach to achieving sustainable and effective electrocatalysis. *J. Environ. Chem. Eng.* **2023**, *11*, 109045. [[CrossRef](#)]
51. Cao, X.; Zhu, L.; Yu, G.; Zhang, X.; Jin, H.; He, D. Visual and colorimetric determination of mercury (II) based on lignosulfonate-capped silver nanoparticles. *Green Chem. Lett. Rev.* **2023**, *16*, 2169590. [[CrossRef](#)]
52. Purnawati, D.; Regonia, P.R.; Bermundo, J.P.; Ikeda, K.; Uraoka, Y. Machine-Learned Fermi Level Prediction of Solution-Processed Ultrawide-Bandgap Amorphous Gallium Oxide (a-Ga₂O_x). *ACS Appl. Electron. Mater.* **2022**, *4*, 5838–5846. [[CrossRef](#)]
53. Stanca, M.; Gaidau, C.; Alexe, C.-A.; Stanculescu, I.; Vasilca, S.; Matei, A.; Simion, D.; Constantinescu, R.-R. Multifunctional leather surface design by using carbon nanotube-based composites. *Materials* **2021**, *14*, 3003. [[CrossRef](#)] [[PubMed](#)]
54. Yao, H.; Wang, S.; Cao, Y.; Chen, R.; Lu, Z.; Hu, J.; Xie, J.; Hao, A. High-performance bifunctional electrocatalysts of CoFe-LDH/NiCo₂O₄ heterostructure supported on nickel foam for effective overall water splitting. *J. Alloys Compd.* **2022**, *926*, 166846. [[CrossRef](#)]
55. Li, C.; Pan, J.; Zhang, L.; Fang, J. Colloidal synthesis of monodisperse trimetallic Pt-Fe-Ni nanocrystals and their enhanced electrochemical performances. *Nanotechnology* **2022**, *34*, 075401. [[CrossRef](#)] [[PubMed](#)]
56. Lu, L.; Zhang, Y.; Chen, Z.; Feng, F.; Ma, Z.; Zhang, S.; An, Q. Elemental diversity-enhanced HER and OER photoelectrochemical catalytic performance in FeCo-AuNP/nitrogen-carbon composite catalysts. *Appl. Surf. Sci.* **2021**, *568*, 151005. [[CrossRef](#)]
57. Jiang, Y.; Sun, P.; Sharma, L.; Mao, B.; Kakkar, R.; Meng, T.; Zheng, L.; Cao, M. Further insights into bifunctional mechanism in alkaline hydrogen evolution for hybridized nanocatalysts and general route toward mechanism-oriented synthesis. *Nano Energy* **2021**, *81*, 105645. [[CrossRef](#)]
58. Zhang, B.; Pan, C.; Liu, H.; Wu, X.; Jiang, H.; Yang, L.; Qi, Z.; Li, G.; Shan, L.; Lin, Y.; et al. Achieving high-efficient urea oxidation via regulating the rate-determining step over a V single atom incorporated Co hydroxide electrocatalyst. *Chem. Eng. J.* **2022**, *439*, 135768. [[CrossRef](#)]

59. Anantharaj, S. Hydrogen evolution reaction on Pt and Ru in alkali with volmer-step promoters and electronic structure modulators. *Curr. Opin. Electrochem.* **2022**, *33*, 100961. [[CrossRef](#)]
60. Díaz-Coello, S.; García, G.; Arévalo, M.C.; Pastor, E. Precise determination of Tafel slopes by DEMS. Hydrogen evolution on tungsten-based catalysts in alkaline solution. *Int. J. Hydrogen Energy* **2019**, *44*, 12576–12582. [[CrossRef](#)]
61. Sarac, B.; Karazehir, T.; Mühlbacher, M.; Sarac, A.S.; Eckert, J. Electrocatalytic behavior of hydrogenated Pd-metallic glass nanofilms: Butler-Volmer, Tafel, and impedance analyses. *Electrocatalysis* **2020**, *11*, 94–109. [[CrossRef](#)]
62. Zhang, C.; Wang, J.; Liu, Y.; Li, W.; Wang, Y.; Qin, G.; Lv, Z. Electrocatalytic HER Enhancement of C₃N₄ in NiCo₂O₄. *Chem.—Asian J.* **2022**, *17*, e202200377. [[CrossRef](#)] [[PubMed](#)]
63. Lu, S.-S.; Zhang, L.-M.; Fan, K.; Xie, J.-Y.; Shang, X.; Zhang, J.-Q.; Chi, J.-Q.; Yang, X.-L.; Wang, L.; Chai, Y.-M.; et al. In Situ formation of ultrathin C₃N₄ layers on metallic WO₂ nanorods for efficient hydrogen evolution. *Appl. Surf. Sci.* **2019**, *487*, 945–950. [[CrossRef](#)]
64. Zhao, Z.; Yang, H.; Zhu, Y.; Luo, S.; Ma, J. Interfacial N-Cu-S coordination mode of CuSCN/C₃N₄ with enhanced electrocatalytic activity for hydrogen evolution. *Nanoscale* **2019**, *11*, 12938–12945. [[CrossRef](#)] [[PubMed](#)]
65. Moradighadi, N.; Nestic, S.; Tribollet, B. Identifying the dominant electrochemical reaction in electrochemical impedance spectroscopy. *Electrochim. Acta* **2021**, *400*, 139460. [[CrossRef](#)]
66. Sengur-Tasdemir, R.; Guler-Gokce, Z.; Sezai Sarac, A.; Koyuncu, I. Determination of membrane protein fouling by UV spectroscopy and electrochemical impedance spectroscopy. *Polym.-Plast. Technol. Eng.* **2018**, *57*, 59–69. [[CrossRef](#)]
67. Wang, X.; Li, Z.; Zhang, J.; Yan, H.; Wang, C.; Wu, F.; Tian, A.; Hong, X.; Dong, W.; Yang, S. Effect of average interlayer spacing on capacitance of NiMn layered double hydroxide. *Chem. Eng. J.* **2020**, *398*, 125618. [[CrossRef](#)]
68. Fang, Q.; Sun, M.; Ren, X.; Sun, Y.; Yan, Y.; Gan, Z.; Huang, J.; Cao, B.; Shen, W.; Li, Z.; et al. MnCo₂O₄/Ni₃S₄ nanocomposite for hybrid supercapacitor with superior energy density and long-term cycling stability. *J. Colloid Interface Sci.* **2022**, *611*, 503–512. [[CrossRef](#)] [[PubMed](#)]
69. Bai, J.; Xue, Q.; Zhao, Y.; Jiang, J.X.; Zeng, J.H.; Yin, S.B.; Chen, Y. Component-dependent electrocatalytic activity of ultrathin PdRh alloy nanocrystals for the formate oxidation reaction. *ACS Sustain. Chem. Eng.* **2018**, *7*, 2830–2836. [[CrossRef](#)]
70. Rao, F.; Ding, K.; Zhou, Y.; Zheng, Y.; Xia, M.; Lv, S.; Song, Z.; Feng, S.; Ronneberger, I.; Mazzarello, R.; et al. Reducing the stochasticity of crystal nucleation to enable subnanosecond memory writing. *Science* **2017**, *358*, 1423–1427. [[CrossRef](#)] [[PubMed](#)]
71. Anand, R.; Nissimagoudar, A.S.; Umer, M.; Ha, M.; Zafari, M.; Umer, S.; Lee, G.; Kim, K.S. Late transition metal doped MXenes showing superb bifunctional electrocatalytic activities for water splitting via distinctive mechanistic pathways. *Adv. Energy Mater.* **2021**, *11*, 2102388. [[CrossRef](#)]
72. Liu, J.; Liu, Y.; Liu, N.; Han, Y.; Zhang, X.; Huang, H.; Lifshitz, Y.; Lee, S.-T.; Zhong, J.; Kang, Z. Metal-free efficient photocatalyst for stable visible water splitting via a two-electron pathway. *Science* **2015**, *347*, 970–974. [[CrossRef](#)] [[PubMed](#)]
73. Fu, L.; Li, Y.; Yao, N.; Yang, F.; Cheng, G.; Luo, W. IrMo nanocatalysts for efficient alkaline hydrogen electrocatalysis. *ACS Catal.* **2020**, *10*, 7322–7327. [[CrossRef](#)]
74. Wang, P.; Shao, Q.; Guo, J.; Bu, L.; Huang, X. Promoting alkaline hydrogen evolution catalysis on P-decorated, Ni-segregated Pt–Ni–P nanowires via a synergetic cascade route. *Chem. Mater.* **2020**, *32*, 3144–3149. [[CrossRef](#)]
75. Creus, J.; Drouet, S.; Surinach, S.; Lecante, P.; Collière, V.; Poteau, R.; Philippot, K.; García-Antón, J.; Sala, X. Ligand-capped Ru nanoparticles as efficient electrocatalyst for the hydrogen evolution reaction. *ACS Catal.* **2018**, *8*, 11094–11102. [[CrossRef](#)]
76. Zhuang, M.; Ou, X.; Dou, Y.; Zhang, L.; Zhang, Q.; Wu, R.; Ding, Y.; Shao, M.; Luo, Z. Polymer-embedded fabrication of Co₂P nanoparticles encapsulated in N, P-doped graphene for hydrogen generation. *Nano Lett.* **2016**, *16*, 4691–4698. [[CrossRef](#)] [[PubMed](#)]
77. Chen, W.; Pei, J.; He, C.T.; Wan, J.; Ren, H.; Zhu, Y.; Wang, Y.; Dong, J.; Tian, S.; Cheong, W.; et al. Rational design of single molybdenum atoms anchored on N-doped carbon for effective hydrogen evolution reaction. *Angew. Chem.* **2017**, *129*, 16302–16306. [[CrossRef](#)]
78. Jiao, L.; Zhou, Y.X.; Jiang, H.L. Metal–organic framework-based CoP/reduced graphene oxide: High-performance bifunctional electrocatalyst for overall water splitting. *Chem. Sci.* **2016**, *7*, 1690–1695. [[CrossRef](#)] [[PubMed](#)]
79. Jin, H.; Wang, J.; Su, D.; Wei, Z.; Pang, Z.; Wang, Y. In situ cobalt–cobalt oxide/N-doped carbon hybrids as superior bifunctional electrocatalysts for hydrogen and oxygen evolution. *J. Am. Chem. Soc.* **2015**, *137*, 2688–2694. [[CrossRef](#)]
80. Yang, L.; Guo, Z.; Huang, J.; Xi, Y.; Gao, R.; Su, G.; Wang, W.; Cao, L.; Dong, B. Vertical growth of 2D amorphous FePO₄ nanosheet on Ni foam: Outer and inner structural design for superior water splitting. *Adv. Mater.* **2017**, *29*, 1704574. [[CrossRef](#)] [[PubMed](#)]
81. Yan, H.; Xie, Y.; Jiao, Y.; Wu, A.; Tian, C.; Zhang, X.; Wang, L.; Fu, H. Holey reduced graphene oxide coupled with an Mo₂N–Mo₂C heterojunction for efficient hydrogen evolution. *Adv. Mater.* **2018**, *30*, 1704156. [[CrossRef](#)] [[PubMed](#)]
82. Zhuang, Z.; Li, Y.; Li, Z.; Lv, F.; Lang, Z.; Zhao, K.; Zhou, L.; Moskaleva, L.; Guo, S.; Mai, L. MoB/g-C₃N₄ interface materials as a schottky catalyst to boost hydrogen evolution. *Angew. Chem.* **2018**, *130*, 505–509. [[CrossRef](#)]
83. Wu, H.B.; Xia, B.Y.; Yu, L.; Yu, X.Y.; Lou, X.W. Porous molybdenum carbide nano-octahedrons synthesized via confined carburization in metal-organic frameworks for efficient hydrogen production. *Nat. Commun.* **2015**, *6*, 6512. [[CrossRef](#)] [[PubMed](#)]

Disclaimer/Publisher’s Note: The statements, opinions and data contained in all publications are solely those of the individual author(s) and contributor(s) and not of MDPI and/or the editor(s). MDPI and/or the editor(s) disclaim responsibility for any injury to people or property resulting from any ideas, methods, instructions or products referred to in the content.